ChemMedChem

Chemistry Europe
European Chemical Societies Publishing

Accepted Article

Title: Xanthenylacetic Acid Derivatives Effectively Target Lysophosphatidic Acid Receptor 6 to Inhibit Hepatocellular Carcinoma Cell Growth

Authors: Davide Gnocchi, Maria M. Cavalluzzi, Giuseppe F. Mangiatordi, Rosanna Rizzi, Cosimo Tortorella, Mauro Spennacchio, Giovanni Lentini, Angela Altomare, Carlo Sabbà, and Antonio Mazzocca

To be cited as: *ChemMedChem* 10.1002/cmdc.202100032

Link to VoR: https://doi.org/10.1002/cmdc.202100032

WILEY-VCH

FULL PAPER WILEY-VCH

Xanthenylacetic Acid Derivatives Effectively Target Lysophosphatidic Acid Receptor 6 to Inhibit Hepatocellular Carcinoma Cell Growth

Davide Gnocchi,[a] Maria M. Cavalluzzi,[b] Giuseppe F. Mangiatordi,[c] Rosanna Rizzi,[c] Cosimo Tortorella,[a] Mauro Spennacchio,[b],[c] Giovanni Lentini,[b] Angela Altomare,[c] Carlo Sabbà,[a] and Antonio Mazzocca *[a]

[a] Dr. D. Gnocchi, Dr. C. Tortorella, Dr. C. Sabbà, Dr. A. Mazzocca
Interdisciplinary Department of Medicine, University of Bari School of Medicine
Piazza G. Cesare, 11 - 70124 Bari, Italy
E-mail: antonio.mazzocca@uniba.it
[b] Dr. M.M. Cavalluzzi, M. Spennacchio, Dr. Giovanni Lentini
Department of Pharmacy - Drug Sciences, University of Bari Aldo Moro
via Orabona, 4 - 70125 Bari, Italy
[c] Dr. G.F. Mangiatordi, Dr. R. Rizzi, Dr. A. Altomare, M. Spennacchio.
Institute of Crystallography – CNR
Via Amendola 122/o – 70126 Bari, Italy

Supporting information for this article is given via a link at the end of the document.

Abstract: Despite the increasing incidence of Hepatocellular carcinoma (HCC) worldwide, current pharmacological treatments are still unsatisfactory. We have previously shown that lysophosphatidic acid receptor 6 (LPAR6) supports HCC growth and that 9-xanthenylacetic acid (XAA) acts as an LPAR6 antagonist inhibiting HCC growth without toxicity. Here, we synthesized four novel XAA derivatives, (±)-2-(9*H*-xanthen-9-yl)propanoic acid (compound **4** – MC9), (±)-2-(9*H*-xanthen-9-yl)butanoic acid (compound **5** – MC6), (±)-2-(9*H*-xanthen-9-yl)hexanoic acid (compound **7** – MC11), and (±)-2-(9*H*-xanthen-9-yl)octanoic acid (compound **8** – MC12, sodium salt) by introducing alkyl groups of increasing length at the acetic α-carbon atom. Two of these compounds were characterized by X-ray powder diffraction and quantum mechanical calculations, while molecular docking simulations suggested their enantioselectivity for LPAR6. Biological data showed anti-HCC activity for all XAA derivatives, with the maximum effect observed for MC11. Our findings support the view that increasing the length of the alkyl group improves the inhibitory action of XAA and that enantioselectivity can be exploited for designing novel and more effective XAA-based LPAR6 antagonists.

Introduction

Today, despite the decline in the incidence of chronic hepatitis infection, hepatocellular carcinoma (HCC) is the sixth leading cause of cancer-related deaths in the world and it is expected to become the third leading cause of cancer-related deaths in Western countries by 2030.[1] The increase in the incidence of metabolic diseases explains this trend. Indeed, recent evidence suggests a correlation between metabolic syndrome, diabetes, obesity, and HCC.[2] The pharmacological treatment of HCC is mainly based on tyrosine kinase inhibitors (i.e., sorafenib, regorafenib, and lenvatinib[2]), alone or combined with immunotherapeutic drugs, such as pembrolizumab and nivolumab.[3] Nevertheless, such approaches are characterized by several unfavorable effects, making them not well tolerated by patients in the long term.[4],[5] Thus, there is an extreme need for new efficient and better-tolerated therapeutics for HCC. The autotaxin-lysophosphatidic acid (ATX-LPA) axis signaling pathway is particularly relevant to HCC development and progression.[6],[7] We previously demonstrated that LPA triggers the trans-differentiation of peritumoral tissue fibroblasts (PTFs) in carcinoma-associated fibroblasts (CAF)[8] and that LPA receptor 6 (LPAR6) promotes HCC tumorigenicity, also worsening clinical consequences in patients.[9] We later showed that 9-xanthenylacetic acid (XAA) inhibits HCC growth without toxic effects by acting as an LPAR6 antagonist.[10]

It has been reported that chirality as well as the increase in the degree of saturation [i.e., sp^3 hybridized carbon atom fraction (Fsp^3)] are positively related to the potential clinical efficiency of new drug candidates.[11] Here, we aimed to explore the effect of the introduction of an alkyl group at the α-position of the XAA carboxyl function on the interaction with LPAR6 and if such modification could result in an improvement in the inhibition of HCC cell growth. Hence, (±)-2-(9*H*-xanthen-9-yl)propanoic acid (compound 4 – MC9), (±)-2-(9*H*-xanthen-9-yl)butanoic acid (compound 5 – MC6), (±)-2-(9H-xanthen-9-yl)hexanoic acid (compound 7 – MC11), and (±)-2-(9H-xanthen-9-yl)octanoic acid (compound 8 – MC12, sodium salt) were synthesized, and structurally characterized by X-ray powder diffraction, submitted to quantum mechanical calculations, and evaluated for their biological activity in inhibiting HCC growth in two different cell lines. Moreover, molecular docking simulations were performed to obtain a reliable working hypothesis about which interactions are critical for molecular recognition in the LPAR6 binding site. These simulations gave interesting insights into the characteristics of the LPAR6 binding site and provided a theoretical basis for further optimization of these compounds.

Results and Discussion

Synthesis of XAA derivatives

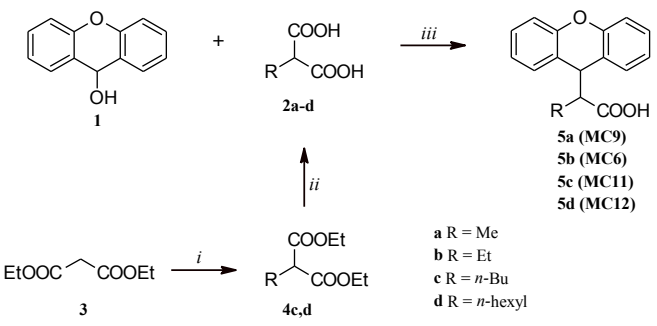

Scheme 1: *Reagents and conditions*: i) suitable alkyl iodide, NaH, THF/DMF, reflux, 24 h; ii) NaOH, H_2O, reflux, 4 h; iii) KOH, pyrrolidine, *i*-PrOH, toluene, reflux, 24 h.

(±)-2-(9*H*-Xanthen-9-yl)alkanoic acids **5a–d** were prepared starting from 9-hydroxyxanthene (**1**) and suitable α-alkyl malonic acids (**2a–d**). Since the previously reported procedure[10] gave very low yield when applied to the synthesis of **5a**, the synthesis of **5a–d** was carried out through alternative experimental conditions that allowed us to ensure higher yields, while avoiding the use of the toxic pyridine as a solvent. Therefore, 9-hydroxyxanthene (**1**) was reacted with **2a–d** in toluene at reflux for 24 h, and pyrrolidine was used as an organocatalyst for the decarboxylative reaction (Scheme 1).[12] In particular, methyl and ethylmalonic acids (**2a** and **2b,** respectively) were commercially available, while *n*-butyl and *n*-hexylmalonic acids (**2c** and **2d**, respectively) were synthesized modifying literature procedures.[12],[13] Diethyl malonate (**3**) was submitted to an alkylation reaction at the alpha carbon with the suitable alkyl iodide[13] to give the intermediates **4c** and **4d** which were in turn hydrolyzed to the corresponding α-alkyl malonic acids[14] (**2c** and **2d**).

Quantum mechanical calculations

The two higher homologs of XAA, namely MC9 and MC6, displayed an increased reluctance to solubilization (data not shown) and this was in line with the corresponding higher lipophilic character (cLog *P* 2.5, 3.0, and 3.5 for XAA, MC9, and MC6, respectively; Spartan'16). The pharmacological activity is expected to increase with lipophilicity in the congeneric series.[11] However, the higher lipophilicity *per se* might not be the only factor affecting any observed hierarchy of activities. Indeed, the alkyl substituents introduced onto the side chain α-position might contribute to the interaction with specific lipophilic residues in the binding site or forcing the orientation of the carboxylic group, a putative pharmacophoric element, to favorable directions. The latter possibility seems to be supported by the characteristic of the ^{1}H NMR signals in the aromatic region (Figure 1), where an increased rigidity of the rotatable bonds might be envisaged as the cause of the progressive alteration of the signal definition and up-field shift, observed when passing from XAA (Figure 1A) to MC6 (Figure 1C) through MC9 (Figure 1B). Indeed, the putative increase in rigidity may also be related to the relatively low solubility observed in MC9.[15]

To gain an in-depth understanding of the effects of α-substitution on the conformational freedom, the analysis of the conformer distribution of the studied compounds was performed together with an optimization of the geometric structure of the corresponding conformers through quantum mechanical calculations (DFT B3LYP/6-31G*//DFT B3LYP/6-31G*, gaseous phase). The study was conducted on both separated enantiomers and, as expected, similar results were obtained for the enantiomers of both MC9 and MC6. For the sake of simplicity, only the S enantiomers of MC9 and MC6 will be discussed. Relatively to the benzo ring, the most stable conformers of the three compounds have the same synclinal and antiperiplanar orientation (Figure 2A and B for MC6). However, a folded, less stable conformer (Figure 2C and D for MC6) was found in the population of each analog (E = 2.0–3.2 kcal/mol, higher than the global minimum conformational isomer energy). Based on the relative Boltzmann weights, this conformer was increasingly more abundant when passing from XAA to MC6 through MC9. Similar results were obtained when running the above geometry optimization on the corresponding ionized structures (XAA, MC9, and MC6 carboxylate anions) applying the conductor-like polarizable continuum model (C-PCM; Spartan'16), to allow for aqueous solvating effect consideration.

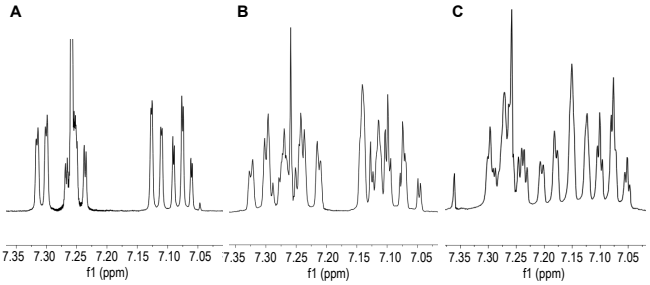

Figure 1. ^{1}H NMR signals in the aromatic region of the spectra of XAA (A), MC9 (B), and MC6 (C).

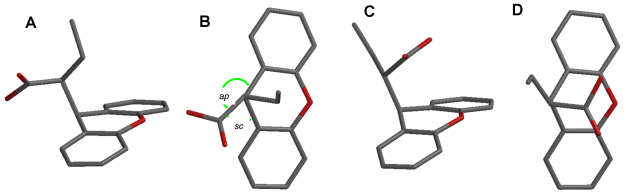

Figure 2. (A, B) Global minimum conformer (DFT B3LYP/6-31G*//DFT B3LYP/6-31G*) of MC6; (C, D) folded conformer of MC6. The views in panels (B) and (D) were obtained observing the models along the *Cα-C9* bond direction. For the sake of clarity, all the hydrogen atoms were removed. Color legend: oxygen (red); carbon (grey).

X-ray powder diffraction

MC6, MC9, and XAA were characterized by X-ray powder diffraction data analysis, and the structure determination process, from pattern indexation to Rietveld refinement,[16] was performed via the EXPO software.[17] The structure solution was obtained in the reciprocal space[18] with Direct Methods for XAA and MC9, and in the direct space[19] by Simulated Annealing algorithm for MC6. The refined molecular structures of XAA, MC9, and MC6 are shown in Figure 3A, B, and C, respectively, resulting in good agreement with the conformer distributions obtained with quantum mechanical calculations (Figure 2). The powder X-ray data collection information, the crystal structure analysis, and the refinement statistics are described in the Experimental Section.

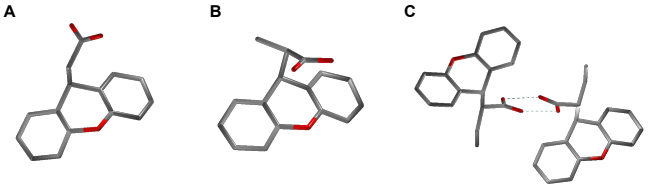

Figure 3. Refined molecular structures in the asymmetric unit: XAA (A), MC9 (B), and MC6 (C). For the MC6 compound, the intermolecular hydrogen bonds are shown. The hydrogen atoms are omitted for clarity. Color legend: oxygen (red); carbon (grey).

Molecular docking

To gain insight into the molecular interactions established by XAA, MC9, MC6, and MC11 in the LPAR6 binding site, we conducted molecular docking simulations. It should be noted that thanks to the recently released first X-ray structure of the zebrafish LPAR6 (PDB code: 5XSZ),[20] reliable docking simulations are now possible. Both enantiomers of MC9, MC6,

and MC11 were considered during the performed simulations and Figure 4 shows the obtained top-scored docking poses.

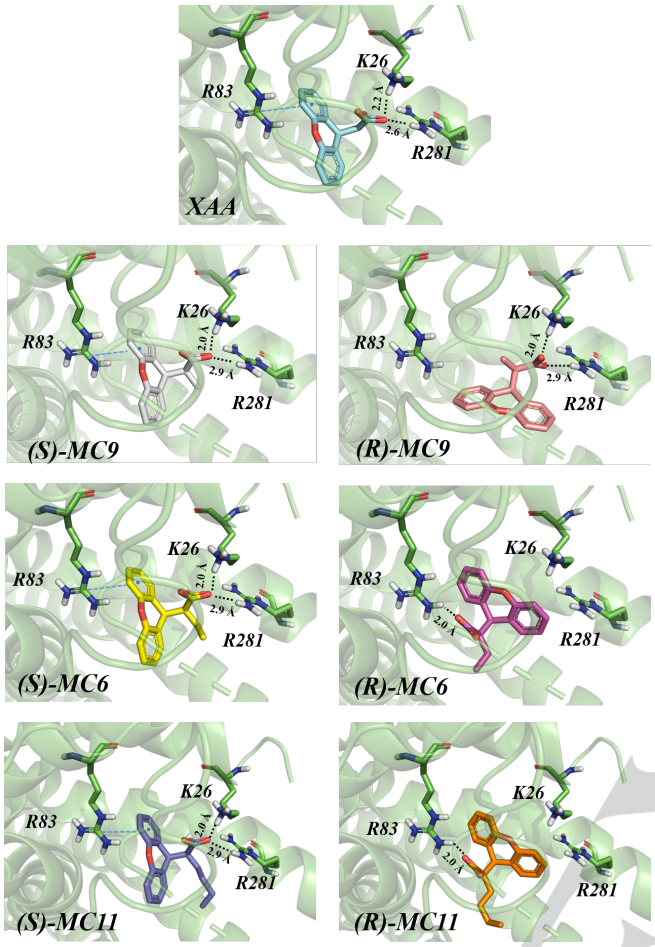

Figure 4. Top-scored docking poses of XAA, (*S*)-MC9, (*R*)-MC9, (*S*)-MC6, (*R*)-MC6, (*S*)-MC11 and (*R*)-MC11. Important residues are represented as sticks, while LPAR6 protein structure is represented as a cartoon. Salt-bridge and cation-pi interactions are depicted by black and cyan dotted lines, respectively.

In particular, the same binding mode is predicted for XAA, (*S*)-MC9, (*S*)-MC6, and (S)-MC11: the negatively charged carboxyl group establishes two salt-bridge interactions with the positively charged side chains of K26 and R281 while the xanthenyl group interacts with R83 *via* cation-pi interaction. Noteworthy, Taniguchi et al.[20] showed that K26, R281, and R83 are residues particularly important for the recognition of the negatively charged phosphate head group of LPA, based on mutagenesis analyses. The authors also performed docking simulations of LPA and hypothesized two possible binding modes, one of which was characterized by two salt bridges involving the phosphate group and both K26 and R281. These lines of evidence strongly support the robustness of the predicted binding mode for XAA, (*S*)-MC9, (*S*)-MC6, and (S)-MC11. Different binding modes are instead predicted for (*R*)-MC9, (*R*)-MC6, and (R)-MC11, thus suggesting that the binding site of LPAR6 is enantioselective. Such a hypothesis is supported by the obtained binding free energies (ΔG_{bind}) computed through MM-GBSA calculations (Table 1). Indeed, (*S*)-MC9 (-47.76 kcal/mol), (*S*)-MC6 (-50.65 kcal/mol) and (S)-MC11 (-50.54 kcal/mol) gave better values of ΔG_{bind} with respect to (*R*)-MC9 (-40.70 kcal/mol), (*R*)-MC6 (-33.89 kcal/mol) and (R)-MC11 (-48.86 kcal/mol) respectively. Last but not least, both (*S*)-MC11 and (R)-MC11 return better ΔG_{bind} than XAA (-46.48 kcal/mol), suggesting that this compound has a higher affinity for LPAR6.

It is worth noting that docking simulations were also performed on both MC12 enantiomers returning a different binding mode, and a lower docking score in comparison with the other XAA derivatives (data not shown). Therefore, the ΔG_{bind} of this compound was not calculated.

Table 1. ΔG_{bind} computed for all the simulated compounds using MM-GBSA calculations.

Compound	ΔG_{bind} (kcal/mol)
XAA	-46.48
(*S*)-MC9	-47.76
(*R*)-MC9	-40.70
(*S*)-MC6	-50.65
(*R*)-MC6	-33.89
(*S*)-MC11	-50.54
(*R*)-MC11	-48.85

Biological findings

Effect of XAA derivatives on HCC cell growth

We tested the effect of XAA, MC9, MC6, MC11, and MC12 in inhibiting HCC cell growth in two different cell lines, Huh7 and HepG2. We took advantage of two different methods: end-point cell counting by Trypan Blue exclusion test and crystal violet staining. Results reported in Figure 5A and B show the following efficacy trend in inhibiting HCC cell growth: MC11> MC6>XAA≥ MC9>MC12, which is consistent with the docking simulation data. This trend is corroborated also by experiments on cell cycle phase distribution reported in Figure 5C, which evidences a cytostatic action due to an arrest in the G1 phase of the cell cycle. Figure 5D reports the IC50 calculated based on the inhibitory activity of XAA derivatives on the growth of HCC cells. We also tested the effect of the two optically active forms of MC9, demonstrating the presence of enantioselectivity and supporting docking simulation studies (Figure 5B).

Since human cancers preferentially grow in acidic conditions, which negatively affect the effectiveness of many anticancer drugs[21],[22],[23], we tested the effect of XAA derivatives in such conditions. We employed an acidic cell culture medium as previously reported.[24] We found that acidic pH did not affect the anti-proliferative effect of XAA derivatives in Huh7 cells, while in HepG2 cells, this effect was reduced (Figure S2).

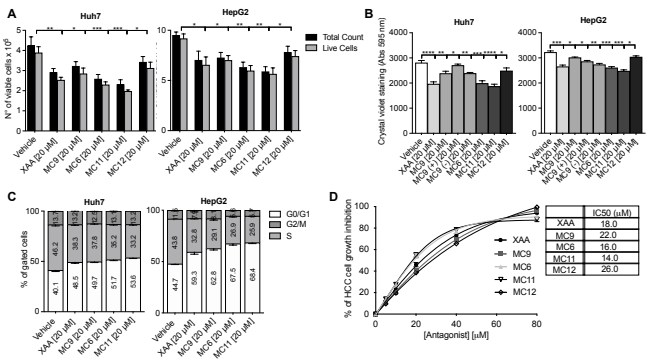

Figure 5. Effect of XAA, MC9, MC6, MC11 and MC12 on HCC cell growth. (A) Effect of XAA, MC9, MC6, MC11 and MC12 on HCC cell growth assessed by end-point cell counting by Trypan Blue exclusion test. *p < 0.05, **p < 0.01, ***p < 0.001 as determined by Two Way ANOVA followed by Dunnett's post-hoc test. Data represent three independent biological replicates performed in

duplicate. (B) Effect of XAA, MC9, MC6, MC11 and MC12 on HCC cell growth assessed by crystal violet staining. *p < 0.05, **p < 0.01, ****p < 0.0001 as determined One-Way ANOVA followed by Dunnett's post-hoc test. Data represent three independent biological replicates performed in duplicate. (C) Effect of XAA, MC9, MC6, and MC11 on cell cycle phase distribution assessed by a cytofluorimetric assay. Data are representative of two independent biological replicates. (D) The IC50 of the pharmacological inhibitory effect of XAA, MC9, MC6, MC11, and MC12 on the growth of HCC cell lines.

Effect of the XAA derivatives on cell toxicity and apoptosis

We then examined the effect of XAA, MC9, MC6, MC11, and MC12 on cell toxicity using two different tests: SRB and MTT. Results reported in Figure 6 A and B show that all three compounds under evaluation exert a similar effect, even if a trend MC11 > MC6 > XAA ≥ MC9 can still be noticed. Also, we evaluated the effect of XAA, MC9, MC6, MC11, and MC12 on cell toxicity and apoptosis using a cytofluorimetric approach, which allows us to discriminate viable, apoptotic, and dead cells, and to determine the number of viable cells. Results reported in Figure 6 C and D illustrate the same trend (MC11 > MC6 > XAA ≥ MC9 > MC12) in the number of viable cells. Moreover, MC6 and MC9 show a similar effect in inducing apoptosis, even if some differences are observable between the two cell lines.

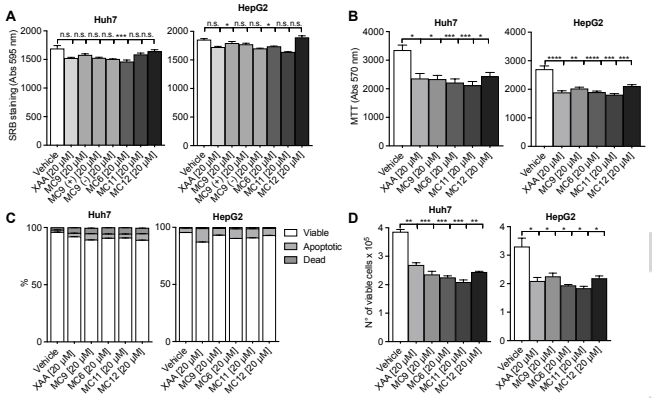

Figure 6. Effect of XAA, MC9, MC6, MC11 and MC12 on HCC cell toxicity. (A) Effect of XAA, MC9, MC6, MC11 and MC12 on HCC cell toxicity assessed by SRB staining test. *p < 0.05 and ***p < 0.001 as determined by One Way ANOVA followed by Dunnett's post-hoc test. n.s. not significative. Data represent three independent biological replicates performed in duplicate. (B) Effect of XAA, MC9, MC6, MC11 and MC12 on HCC cell toxicity assessed by MTT staining test. *p < 0.05, **p < 0.01, ***p < 0.001, ****p < 0.0001 as determined One-Way ANOVA followed by Dunnett's post-hoc test. Data represent three independent biological replicates performed in duplicate. (C) and (D) Effect of XAA, MC9, MC6, MC11 and MC12 on cell toxicity and cell death as assessed by cytofluorimetric approach. *p < 0.05, **p < 0.01, ***p < 0.001 as determined One-Way ANOVA followed by Dunnett's post-hoc test. Data represent two independent biological replicates.

Owing to the high incidence of HCC and the lack of adequate pharmacological approaches, the identification of novel molecules capable of effectively inhibit LPAR6-driven HCC growth with fewer side effects compared to the currently available therapeutic approaches would be of high relevance. In the search for novel LPAR6 antagonists, we recently identified 9-xanthenylacetic acid (XAA), which showed significant anti-proliferative effects both *in vitro* and *in vivo* at therapeutic doses without significant toxicity.[10] In this context, our work aimed to synthesize, characterize, and study the biological effects of four new XAA derivatives, namely (±)-2-(9*H*-xanthen-9-yl)propionic acid (compound **4** - MC9), (±)-2- (9*H*-xanthen-9-yl)butyric acid (compound **5** - MC6), (±)-2-(9*H*-xanthen-9-yl)hexanoic acid (compound **7** – MC11), and (±)-2-(9*H*-xanthen-9-yl)octanoic acid (compound **8** – MC12, sodium salt) as LPAR6 antagonists with antitumor activity in HCC. In all the biological tests conducted in this study, we obtained data that highlighted a trend in the biological activity of these antagonists, namely MC6 > XAA ≥ MC9. Therefore, extending the length of the alkyl group on the α-carbon of acetic acid improves the antagonistic activity of XAA on LPAR6, thereby enhancing the effect of inhibiting the growth of HCC cells. Nevertheless, the activity of MC9 is comparable to XAA and this can be explained with the enantioselectivity of LPAR6, as shown by docking simulation studies. The ^{1}H-NMR spectra recorded on the studied compounds point to possible steric hindrance effects exerted by the α-substituent on the rotation of the *Cα–C*9 bond. Quantum mechanical calculations indicated two common possible conformations as the most stable both in the gaseous and aqueous phases. The most stable one presents the carboxyl group antiperiplanar to one benzene ring and synclinal to the other. The second conformation resulted to be folded so that the carboxyl group is suspended on the planar moiety of the compounds. Interestingly, the two most stable conformations are unambiguously confirmed by the crystal structures as obtained by X-ray powder diffraction data analysis (Figure 3), also supporting as the compounds under investigation assume the same conformation in the solid-state as in the gaseous and aqueous phase. The folded conformer represents only a small fraction in the conformer distribution (less than 2%). However, this relatively unstable conformation was two times more probable in MC6 distribution than in the distribution of MC9 and XAA. This observation may suggest that increasing the size of the alkyl substituent in the alpha-position of the side chain results in increased pharmacological activity if the increased size of the substituents would further increase the probability of the existence of the putatively "right" conformation in the population of the so-obtained congeners. Of course, an increase in the size of the substituent should increase lipophilicity and contribute positively to potency. Finally, it should not be overlooked the possibility that the so-obtained congeners may better fit the binding site by interacting with further lipophilic residues therein. It should be noted that the efficacy of MC12 is lower than that of other derivatives, which indicates that further increasing the length of the alkyl group does not lead to an increase in inhibitory activity. This effect may be due to steric hindrance.

The picture that emerged from molecular docking simulations is consistent with the experimental findings and suggests two salt-bridge interactions with the positively charged side chains of K26 and R281 and a cation-pi interaction involving the xanthenyl group and R83 as crucial for the binding of our derivatives towards LPAR6. It is worth mentioning here that all these residues are fully conserved among different species.[20] Moreover, it must be pointed out that for MC6, MC9, and MC11, the top MM-GBSA scored pose was that returned by the S-enantiomer, thus indicating that the interactions taking place at the binding pocket could be stereoselective. Based on these data, important clues for designing higher affinity ligands can be derived. In particular, we can here hypothesize that molecular recognition benefits from the presence of polar or charged substituents on the xanthenyl group, which can interact with R83 through H bonds or salt bridge interactions.

Conclusion

Hepatocellular carcinoma (HCC) is an emerging and severe disease with a worldwide epidemiological diffusion. So far, the pharmacological approaches available against HCC show limited efficacy and evident side effects. Here, we presented four novel xanthenylacetic acid (XAA) derivatives, MC9 (compound 4), MC6 (compound 5), MC11 (compound 7) and MC12 (compound 8), obtained by increasing the length of the alkyl group at the acetic α-carbon atom. By using docking simulations, we speculated that the binding of MC9, MC6, MC11, and MC12 can be enantioselective. The biological data presented in this

study on MC9, MC6, MC11, and MC12 are consistent with docking simulation data, thus corroborating their robustness. Moreover, we showed that the inhibitory activity is not maximized in MC12, indicating that further increasing the length of the alkyl group will not lead to an improvement of the inhibitory activity. Therefore, our results provide novel insights for the design of novel LPAR6 antagonists with specific translational potential. Also, our observations lay the foundation and open the way for further improvements in the design of new and more efficient LPAR6 antagonists. Indeed, our research is now aimed to design and test novel XAA derivatives with different groups. We provided evidence on the chemical and physical properties of novel LPAR6 antagonists, thus paving the way for the development of new pharmacological agents for HCC. This will help expanding the therapeutic arsenal available against HCC.

Experimental Section

Chemistry part. All chemicals were purchased from Sigma-Aldrich in the highest quality commercially available. Solvents were RP grade unless otherwise indicated. Yields refer to purified products and were not optimized. The structures of the compounds were confirmed by routine spectrometric analyses. Melting points were determined on a Gallenkamp melting point apparatus in open glass capillary tubes and are uncorrected. ^{1}H NMR and ^{13}C NMR spectra were recorded on a Varian Mercury-VX spectrometer operating at 300 and 75 MHz for ^{1}H and ^{13}C, respectively, or an AGILENT 500 MHz operating at 500 and 125 MHz for ^{1}H and ^{13}C, respectively, using $CDCl_3$ as the solvent, unless otherwise indicated. Chemical shifts are reported in parts per million (ppm) relative to solvent resonance: $CDCl_3$, δ 7.26 (^{1}H NMR), and δ 77.3 (^{13}C NMR). J*J* values are given in Hz. EIMS spectra were recorded on a Hewlett-Packard 6890-5973 MSD gas chromatograph/mass spectrometer at low resolution. Elemental analyses were performed on a Eurovector Euro EA 3000 analyzer. TLC analyses were performed on precoated silica gel on aluminum sheets (Kieselgel 60 F254, Merck).

General procedure for the synthesis of (±)-2-(9*H*-xanthen-9-yl)alkanoic acids (5a–d)
The method adopted for the synthesis of (±)-2-(9*H*-xanthen-9-yl)propanoic acid (**5a**, **MC9**) is described. Methylmalonic acid (**2a**) (595 mg, 5.04 mmol), KOH (10 mg, 0.16 mmol), pyrrolidine (54 mg, 0.76 mmol), and isopropyl alcohol (30 mg, 0.50 mmol) were added to a stirred solution of 9*H*-xanthen-9-ol (**1**) (500 mg, 2.52 mmol) in toluene (8 mL). The reaction mixture was heated to reflux for 24 h and then cooled to room temperature. The mixture was extracted with a saturated solution of sodium carbonate (3 × 10 mL). After adjusting pH to 1–2 with 6 M HCl, the aqueous phase was extracted with ethyl acetate (3 × 30 mL). The combined organic phases were dried over anhydrous Na_2SO_4 and the solvent removed under reduced pressure to give the desired compound (**5a**) as a brown solid (0.634 g, 99%) which was recrystallized from EtOAc/hexane (49%): mp 124–125 °C; ^{1}H NMR (300 MHz): *δ* 0.92 (d, *J* = 7.0 Hz, 3H, C*H*$_3$), 2.65–2.80 (m, 1H, C*H*CH$_3$), 4.60 (d, *J* = 5.3 Hz, 1H, C*H*Ar), 7.04–7.15(m, 4H, Ar), 7.20–7.35 (m, 4H, Ar); ^{13}C NMR (75 MHz): *δ* 11.5 (1C), 41.6 (1C), 48.4 (1C), 116.5 (2C), 121.4 (1C), 123.2 (1C),123.5 (1C), 123.8 (1C), 128.1 (1C), 128.3 (1C), 128.5 (1C), 129.0 (1C), 152.9 (1C), 153.1 (1C), 179.3 (1C); GC-MS (70 eV) *m/z* (%) 254 (M$^+$, <1), 181 (100). Anal. ($C_{16}H_{14}O_3 \cdot 0.2H_2O$) C, H.

(±)-2-(9*H*-Xanthen-9-yl)butanoic acid (**5b, MC6**)
Prepared as reported for **5a** starting from **1** and ethylmalonic acid (**2b**). The desired product (**5b**) was obtained as a pale green solid (80%) which was recrystallized from toluene/hexane (30%): mp 115–116 °C; ^{1}H NMR (300 MHz): *δ* 0.81 (t, *J* = 7.4 Hz, 3H, C*H*$_3$), 1.30–1.44 (m, 1H, C*H*HCH$_3$), 1.45–1.58 (m, 1H, CH*H*CH$_3$), 2.46–2.54 (m, 1H, C*H*CH$_2$), 4.30 (d, *J* = 7.0 Hz, 1H, C*H*Ar), 7.05–7.20 (m, 4H, Ar*H*), 7.22–7.35 (m, 4H, Ar*H*); ^{13}C NMR (75 MHz): *δ* 12.0 (1C), 21.3 (1C), 42.2 (1C), 55.7 (1C), 112.5 (1C), 116.6 (1C), 122.6 (1C), 123.0 (1C), 123.4 (1C), 124.2 (1C), 128.1 (1C), 128.2 (1C), 128.4 (1C), 129.3 (1C), 153.0 (1C), 153.1 (1C), 178.6 (1C); GC-MS (70 eV) *m/z* (%) 268 (M$^+$, <1), 181 (100). Anal. ($C_{17}H_{16}O_3 \cdot 0.2H_2O$) C, H.

(±)-2-(9*H*-Xanthen-9-yl)hexanoic acid (**5c, MC11**)
Prepared as reported for **5a** starting from **1** and butylmalonic acid (**2c**). After purification of the crude by column chromatography on silica gel (EtOAc/hexane, 2:8), the desired product (**5c**) was obtained as a pale brown solid (85%): mp 131–133 °C; ^{1}H NMR (500 MHz): δ 0.77 (t, *J* = 7.2 Hz, 3H, C*H*$_3$), 1.02–1.35 (m, 5H, 2 × C*H*$_2$ + C*H*HCH), 1.48–1.56 (m, 1H, CH*H*CH), 2.55–2.60 (m, 1H, C*H*CH$_2$), 4.31 (d, *J* = 7.1 Hz, 1H, C*H*Ar), 7.09 (apparent t, 2H, Ar*H*), 7.15 (d, *J* = 8.2 Hz, 2H, Ar*H*), 7.20 (dd, *J* = 7.5, 1.4 Hz, 1H, Ar*H*), 7.25–7.30 (m, 3H, Ar*H*); ^{13}C NMR (125 MHz): δ 13.9 (1C), 22.6 (1C), 27.9 (1C), 29.8 (1C), 42.5 (1C), 54.2 (1C), 116.7 (1C), 116.8 (1C), 122.7 (1C), 123.2 (1C), 123.6 (1C), 124.3 (1C), 128.3 (1C), 128.4 (1C), 128.6 (1C), 129.5 (1C), 153.19 (1C), 153.20 (1C), 180.4 (1C); HRMS (ESITOF) m/z [M – H]$^-$ calcd for $C_{19}H_{19}O_3$: 295.1340; found 295.1338. Anal. ($C_{19}H_{20}O_3 \cdot 0.25H_2O$) C, H.

(±)-2-(9*H*-Xanthen-9-yl)octanoic acid (**5d, MC12**)
Prepared as reported for **5a** starting from **1** and hexylmalonic acid (**2d**). The desired product (**5d**) was obtained as a brown oil (47%) which was converted into its sodium salt (pale brown waxy solid): ^{1}H NMR (500 MHz, CD_3OD): δ 0.80 (t, *J* = 7.3 Hz, 3H, C*H*$_3$), 1.05–1.10 (m, 4H, 2 × C*H*$_2$), 1.16–1.20 (m, 2H, C*H*$_2$), 1.30–1.32 (m, 3H, C*H*$_2$ + C*H*HCH), 1.40–1.46 (m, 1H, CH*H*CH), 2.26–2.30 (ddd, *J* = 11.1, 7.8, 3.4 Hz, 1H, C*H*CH$_2$), 4.23 (d, *J* = 7.7 Hz, 1H, C*H*Ar), 7.02–7.06 (m, 4H, Ar*H*), 7.15–7.22 (m, 2H, Ar*H*), 7.27 (dd, *J* = 7.6, 1.0 Hz , 1H, Ar*H*), 7.43 (dd, *J* = 7.6, 1.0 Hz, 1H, Ar*H*); ^{13}C NMR (125 MHz, CD_3OD): δ 14.4 (1C), 23.6 (1C), 29.1 (1C), 30.1 (1C), 30.4 (1C), 32.8 (1C), 44.1 (1C), 59.0 (1C), 116.9 (1C), 117.0 (1C), 123.6 (1C), 124.3 (1C), 125.6 (1C), 128.0 (1C), 128.3 (1C), 128.5 (1C), 130.1 (1C), 131.2 (1C), 154.3 (1C), 154.5 (1C), 182.1 (1C); HRMS (ESITOF) m/z [M – H]$^-$ calcd for $C_{21}H_{24}O_3$: 323.1653; found 323.1648. Anal. ($C_{21}H_{23}NaO_3 \cdot 1.33H_2O$) C, H.

General procedure for the synthesis of *n*-alkylmalonic acids (4c,d)
The method adopted for the synthesis of *n*-butylmalonic acid (**4c**) is described. NaH (600 mg, 25.0 mmol) was suspended in a mixture of THF and DMF (3:1, 40 mL). Diethyl malonate **3** (2.0 g, 1.9 mL, 12.5 mmol) was added dropwise and the solution was stirred for 15 min at room temperature. 1-Iodobutane (2.53 g, 1.6 mL, 13.7 mmol) was added and the mixture heated to reflux for 24 h. Then, the mixture was allowed to cool and the solvent was removed under reduced pressure. The residue was poured into water (20 mL) and extracted with diethyl ether (3 × 25 mL). The organic layer was dried over anhydrous Na_2SO_4 and the solvent was removed under reduced pressure affording a yellow oil which was used for the next step without further purification.
Diethyl butylmalonate **4c** (2.46 g, 11.38 mmol) was added to a stirred solution of sodium hydroxide (2.46 g, 61.5 mmol) in water (7 mL). The reaction mixture was heated to reflux for 4 h, then cooled to room temperature. 2 M HCl was added and the aqueous layer was extracted with ethyl acetate (3 × 25 mL). The organic layer was washed with brine, dried over anhydrous Na_2SO_4, and concentrated under reduced pressure. Hexane (30 mL) was added to the residue and the solution was stirred for 3 h. The product was isolated by filtration and dried under reduced pressure affording **4c** (1.43 g, 71%) as a white solid: m.p. 102–104 °C; ^{1}H NMR (500 MHz): δ 0.92 (t, *J* = 7.1 Hz, 3H, C*H*$_3$), 1.36–1.39 (m, 4H, 2 × C*H*$_2$), 1.92–1.98 (m, 2H, C*H*$_2$CH), 3.44 (t, *J* = 7.4 Hz, 1H, C*H*); HRMS (ESITOF) m/z [M + 2Na + H]$^+$ calcd for $C_7H_{11}Na_2O_4^+$ 205.0447; found 205.0448.

n-Hexylmalonic acid (**4d**)
Prepared as reported for **4c** starting from **3** and 1-iodohexane as a gray solid: m.p. 106–108 °C; ^{1}H NMR (300 MHz): δ 0.88 (t, *J* = 6.6 Hz, 3H, C*H*$_3$), 1.25–1.35 (m, 8H, 4 × C*H*$_2$), 1.92–1.98 (m, 2H, C*H*$_2$CH), 3.44 (d, *J* = 7.3 Hz , 1H, C*H*); HRMS (ESITOF) m/z [M – H]$^-$ calcd for $C_9H_{15}O_4^-$ 187.0976; found 187.0968.

X-ray powder diffraction: data collection, structure determination, and refinement. To complete the study and validate the reliability of quantum mechanical analysis results, crystallography studies of structural characterization of XAA, MC9, and MC6 compounds were performed by using X-ray powder diffraction data. All the patterns were collected at room temperature by using an automated Rigaku RINT2500 laboratory diffractometer (50 kV, 200 mA) equipped with the silicon strip Rigaku D/teX Ultra detector. An asymmetric Johansson Ge[111] crystal was used to select the monochromatic Cu Kα_1 radiation (λ=1.54056 Å). The angular range 6°-95° (2θ) for MC6 and 7°–80° (2θ) for XAA and

MC9 was scanned with a step size of 0.02° (2θ) and counting time of 6 s/step. The measurements were executed in transmission mode, by introducing the sample in a special glass capillary with a 0.5 mm diameter and mounted on the axis of the goniometer. To reduce the possible preferred orientation effects, the capillary was rotated during the measurement to improve the randomization of the orientations of the individual crystallites. The main acquisition parameters are reported in Table S1 of the Supplementary Materials.
The collected data were investigated via the EXPO software[17] in a completely automatic way, performing the pathway of a typical polycrystalline structure determination process. It consists of the calculation of the unit cell parameters, the identification of the space group, the structure solution, and the structure model refinement via the Rietveld method.[16] Each diffraction pattern was indexed using N-TREOR09,[25] software integrated into EXPO, by selecting and fitting the first 25 low-angle well-defined peaks of the powder pattern. The unit cell parameters with the largest figures of merit [M(20 = 68, 45, and 34, for XAA, MC9, and MC6, respectively] indexed all the peaks with an orthorhombic cell. Systematic absences suggested the space group $P2_12_12_1$ for XAA, *Pbcn* for MC9, and $Pna2_1$ for MC6, as the most probable ones.
By using EXPO, the crystal structure determination process was approached in the reciprocal space[18] by Direct Methods (DM) for XAA and MC9 samples and in the direct space[19] via Simulated Annealing (SA) global optimization algorithm for MC6.
DM are probabilistic approaches, based on two main steps: 1) the decomposition of the experimental profile for extracting the integrated intensities; 2) the solution of the *phase problem*. For the compounds under investigation, the molecular structure determination process required no default runs of EXPO, and all the obtained final DM models, being approximate, were submitted to model optimization procedures. They are integrated into EXPO as non-standard strategies and are aimed at improving the structural model recovering the missed atoms, removing occurred false positions, and locating atom peaks in better positions.[26],[27]
About MC6, the structure solution was performed in *the* $Pna2_1$ space group, implying the presence of two crystallographically independent molecules in the asymmetric unit. Due to a large number of atoms (40 non-hydrogen atoms), DM are not able to find a correct and complete final model and the structure was solved using the SA algorithm as implemented in the EXPO software.
The method is based on the minimization of the difference between observed and calculated intensities moving, within the unit cell, an expected molecular model by varying its position, orientation, and conformation. The angular range $6° < 2\theta < 45.30°$ (2.0 Å of resolution) was used. The starting expected model of MC6 was assembled using the sketching facilities of ACD/ChemSketch (ACD/ChemSketch: http://www.acdlabs.com/resources/freeware/chemsketch/) and the geometry was optimized by using MOPAC (J.J.P. Stewart, MOPAC2016. Stewart Computational Chemistry (Colorado, CO, USA, Springs), 2016. http://OpenMOPAC.net). A total of 17 parameters were optimized by EXPO during the minimization process: five coordinates to describe the position of the centers of mass, six angles describing the orientation, and six torsion angles to describe the conformation. The algorithm was run 20 times and the best solution with the lowest cost function R_{wp} = 5.79 was selected. The criterion to accept the solution was based also on the soundness of the crystal packing. Direct Methods also confirmed the solution achieved by the real space method.[28]
The obtained crystal structure solutions were supplied as a starting model to the Rietveld refinement. All H atoms attached to C atoms were treated as riding, with Uiso(H) = 1.2Uiso(C) of the carrier atoms. The peak shapes were modeled using the Pearson VII function. The atomic displacement parameters were refined isotropically and constrained to have the same value for atoms of the same chemical element.
In Supplementary Materials, the detailed crystallographic results together with the crystal structure refinement data are reported in Table S1 while in Figure S1, and only for MC6 structure, the final Rietveld plot is displayed.
Further details of the crystal structure investigations may be obtained from the joint CCDC/FIZ Karlsruhe online deposition service: https://www.ccdc.cam.ac.uk/structures/ by quoting the deposition number CCDC-1996157 for XAA, CCDC-1996155 for MC9, and CCDC-1996154 for MC6.

Biological studies

Cell lines and cell culture. HepG2 and Huh7 cell lines were purchased from JCRB Cell Bank. HepG2 and Huh7 were grown in DMEM [Corning cat. # 10-014-CVR] supplemented with 10% FBS [Corning cat. # 35-079-CV]. Compounds used were diluted in DMSO [Corning cat. # 25-950-CQC] and treatments were performed using volumes not exceeding 1% volume of the cell culture media. DMSO was used as vehicle control at 0.5% or 1% volume of cell culture media.

Cell proliferation assays. End-point proliferation was assayed by Crystal Violet staining 72 hours after drug incubation. Crystal Violet [Sigma-Aldrich cat. #C3886] was diluted in EtOH/H_2O 10% v/v to obtain a 1 mg/mL solution, which was added to cells after fixation in 4% paraformaldehyde. The color was eluted with 10% acetic acid and absorbance was read at λ=595 nm using an iMark™ plate reader [Bio-Rad cat. #168-1135].

Cell cycle analysis. Cell cycle analysis was performed using a Guava EasyCyte benchtop flow cytometer [Merck cat. #0500-5009] employing the "Guava Cell Cycle Assay" kit [Merck cat. #4500-0220]. Samples were prepared following the producers' instructions. Briefly, cells were serum-starved for 24 h when ≅ 30%-35% confluent and therefore treated with the specified stimuli for the reported times. After culture media were harvested, cells were washed twice with PBS, which was then collected to have the whole cell population. Cells were then detached from culturing support using trypsin and added to the collected media and PBS. After centrifugation, cells were resuspended in PBS+2%FBS to carefully remove culturing media, centrifuged again, and resuspended in 200 μL PBS+2%FBS. This cell suspension was then poured dropwise into ice-cold 70% ethanol for fixation and permeabilization. After a minimum of 24 h fixation at 4° C, ethanol was removed by centrifugation and, after PBS washings, the reagent was added. Data were acquired after 30 min incubation in the dark.

Toxicity assays. Sulforhodamine B (SRB) assay was performed using a commercial kit following the producer's directions of use [Canvax cat. #CA050]. For MTT [SIGMA cat. #M2128] assay, a 5 mg/mL solution in DPBS was added to the culture media (10% v/v). After 4 h incubation at 37°C, the color was eluted with an acidified isopropanol solution with 1% Triton X-100 (0.1 M HCl in isopropanol 100%+Triton X-100 [Sigma-Aldrich cat. #T9284]). Absorbance was measured using an iMark plate reader at λ=570 nm.
All of the toxicity assays were performed 48 h after adding treatments.

Determination of cell number, cell viability, and apoptosis. The determination of cell number, cell viability, and apoptosis was performed using a Guava EasyCyte benchtop flow cytometer [Merck cat. #0500-5009] using the Guava ViaCount reagent [Merck cat. #4000-0040] following producers' directions of use. This reagent allows a quantitative evaluation of cell number, viability, and apoptosis by discriminating viable and non-viable cells exploiting differential permeability properties of two DNA-binding dyes. The nuclear dye stains only nucleated cells, whereas the viability of dye stains dying cells. This permits us to distinguish viable, apoptotic, and dead cells. Debris is excluded based on negative staining with the nuclear dye. Briefly, cells were treated with the indicated stimuli for the indicated times. Cells were then detached from culturing support by using trypsin, and 50 μL of cell suspension was added to 450 μL of reagent. After 10 minutes of incubation in the dark, data were acquired.
Assays were performed 48 h after adding treatments.

Statistical analyses. In all other experiments, One-Way ANOVA followed by Dunnett's post-hoc test determined statistical significance. Normality was preliminary checked with D'Agostino-Pearson's Omnibus K2 test.
The normality of data was preliminary verified with D'Agostino-Pearson's Omnibus K2 test. One-Way ANOVA followed by Dunnett's post-hoc test was used to determine statistical significance when data were normally distributed. Otherwise, statistical significance was determined by the Kruskal-Wallis test followed by Dunn's multiple comparisons test. Statistical analyses and graphs were performed with Graphpad Prism 9 software.

Docking simulations. Compounds XAA, MC9, MC6 and MC11 were docked on the recently published crystal structure of zebrafish LPAR6 (PDB code: 5XSZ).[20] Both enantiomers of MC9, MC6 and MC11 were considered during the performed simulations. The retrieved .pdb file was prepared using Protein Preparation Wizard, available in the Schrödinger Suite 2019-3 for adding missing hydrogen atoms, reconstructing incomplete side chains, and assigning favorable protonation states at physiological pH [Schrödinger Release 2029-3: Protein Preparation Wizard; Epik, Schrödinger, LLC, New York, NY, 2020; Impact, Schrödinger, LLC, New York, NY, 2020; Prime, Schrödinger, LLC, New York, NY, 2019]. To generate all the possible tautomers and ionization states at a pH value of 7.0 ± 2.0, the ligands were prepared using LigPrep, available in the Schrödinger Suite 2019-3 [Schrödinger Release

2019-3: LigPrep, Schrödinger, LLC, New York, NY, 2019]. The obtained files were used for docking simulations performed by Grid-based ligand docking with energetics (GLIDE) [Schrödinger Release 2019-3: Glide, Schrödinger, LLC, New York, NY, 2019]. During the docking process, full flexibility was allowed for the ligands while the protein was held fixed. The default Force Field OPLS_2005[29] and the standard precision (SP) protocol were employed. A cubic having an edge of 12 Å for the inner box and 32 Å for the outer box and centered on the residues K26, R83, R267 and R281 were employed.

MM-GBSA calculations. The binding free energies (ΔG_{bind}) between protein and ligands were computed by applying the Molecular Mechanics/Generalized Born Surface Area (MM-GBSA)[30] calculations on the obtained top-scored docking poses. More specifically, we employed Prime software, available in the Schrodinger Suite 2019-3 [Schrödinger Release 2020-3: Prime, Schrödinger, LLC, New York, NY, 2020], applying the following Equation:

$$\Delta G_{bind} = \Delta E_{MM} + \Delta G_{solv} + \Delta G_{SA}$$

where ΔE_{MM}, ΔG_{solv}, and ΔG_{SA} represent the difference between the contribution made by the ligand-protein complex and the sum of those made by the ligand and the protein taken alone, in terms of minimized energy, solvation energy, and surface area energy, respectively. Flexibility was allowed to all the residues having at least one atom within a distance of 5 Å for the ligand.

Quantum mechanical calculations. Calculations were performed according to procedures we previously developed.[31] Briefly, the models of the undissociated compounds XAA, MC9, and MC6 were generated from the atomic fragments incorporated into Spartan'16 (Wavefunction Inc., Irvine, CA) inner fragment library and assuming the suggested default starting geometries. The generated geometries were optimized by the molecular mechanics MMFF routine offered by the software[32] and then submitted to a systematic conformational distribution analysis using the default step sizes. All conformers in a window of 10 Kcal/mol above the global minimum conformer were retained. When two conformers differed by dihedral values lower than 10°, the less stable conformer was left out. Conformers were then classified according to their ab initio gas-phase energy content calculated at the RHF/6-31G* level. All conformers falling within a window of 5 kcal/mol above the global minimum were retained and submitted to RHF/6-31G* geometry optimization. After removal of redundant conformers (i.e., each conformer differing from a more stable one by less than 5° in their corresponding dihedral values), the so-obtained set of conformers underwent geometry optimization by density functional theory (DFT) implemented in Spartan'16 with B3LYP functional[33] and the 6-31G* basis setw[34] in the gas phase. The optimized structures were confirmed as real minima by IR frequency calculation (DFT B3LYP/6-31G*//DFT B3LYP/6-31G*). The above geometry optimization was performed also on XAA, MC9, and MC6 carboxylate anions applying the conductor-like polarizable continuum model (C-PCM; Spartan'16) to allow for aqueous solvating effect consideration.[35],[36]

Acknowledgements

We are grateful to Ms. Loredana Angela Acquaro and Dr. Filippo Capodiferro for their technical support.

Keywords: drug design • enantioselectivity • hepatocellular carcinoma • lysophosphatidic acid receptor 6 antagonists • therapeutic tools

[1] C. R. de Lope, S. Tremosini, A. Forner, M. Reig, J. Bruix, *J Hepatol* **2012**, *56 Suppl 1*, S75-87.
[2] A. Forner, M. Reig, J. Bruix, *Lancet* **2018**.
[3] M. Kudo, *Cancers (Basel)* **2018**, *10*(11).
[4] O. Waidmann, *Expert Opin Biol Ther* **2018**, *18*(8), 905-910.
[5] Z. Wu, L. Lai, M. Li, L. Zhang, W. Zhang, *Medicine (Baltimore)* **2017**, *96*(51), e9431.
[6] E. Kaffe, A. Katsifa, N. Xylourgidis, I. Ninou, M. Zannikou, V. Harokopos, P. Foka, A. Dimitriadis, K. Evangelou, A. N. Moulas, U. Georgopoulou, V. G. Gorgoulis, G. N. Dalekos, V. Aidinis, *Hepatology* **2017**, *65*(4), 1369-1383.
[7] S. Nakagawa, L. Wei, W. M. Song, T. Higashi, S. Ghoshal, R. S. Kim, C. B. Bian, S. Yamada, X. Sun, A. Venkatesh, N. Goossens, G. Bain, G. Y. Lauwers, A. P. Koh, M. El-Abtah, N. B. Ahmad, H. Hoshida, D. J. Erstad, G. Gunasekaran, Y. Lee, M. L. Yu, W. L. Chuang, C. Y. Dai, M. Kobayashi, H. Kumada, T. Beppu, H. Baba, M. Mahajan, V. D. Nair, M. Lanuti, A. Villanueva, A. Sangiovanni, M. Iavarone, M. Colombo, J. M. Llovet, A. Subramanian, A. M. Tager, S. L. Friedman, T. F. Baumert, M. E. Schwarz, R. T. Chung, K. K. Tanabe, B. Zhang, B. C. Fuchs, Y. Hoshida, C. Precision Liver Cancer Prevention, *Cancer Cell* **2016**, *30*(6), 879-890.
[8] A. Mazzocca, F. Dituri, L. Lupo, M. Quaranta, S. Antonaci, G. Giannelli, *Hepatology* **2011**, *54*(3), 920-930.
[9] A. Mazzocca, F. Dituri, F. De Santis, A. Filannino, C. Lopane, R. C. Betz, Y. Y. Li, N. Mukaida, P. Winter, C. Tortorella, G. Giannelli, C. Sabba, *Cancer Res* **2015**, *75*(3), 532-543.
[10] D. Gnocchi, S. Kapoor, P. Nitti, M. M. Cavalluzzi, G. Lentini, N. Denora, C. Sabba, A. Mazzocca, *J Mol Med (Berl)* **2019**.
[11] M. M. Cavalluzzi, G. F. Mangiatordi, O. Nicolotti, G. Lentini, *Expert Opin Drug Discov* **2017**, *12*(11), 1087-1104.
[12] S. J. Pridmore, J. M. J. Williams, *Tetrahedron Lett* **2008**, *49*(52), 7413-7415.
[13] C. Bruno, A. Catalano, J. F. Desaphy, M. M. Cavalluzzi, A. Carocci, A. Dipalma, C. Franchini, G. Lentini, D. C. Camerino, V. Tortorella, *Heterocycles* **2007**, *71*(9), 2011-2026.
[14] S. Yang, W. Shi, D. Xing, Z. Zhao, F. Lv, L. Yang, Y. Yang, W. Hu, *Eur J Med Chem* **2014**, *86*, 133-152.
[15] J. Huuskonen, D. J. Livingstone, D. T. Manallack, *Sar and Qsar in Environmental Research* **2008**, *19*(3-4), 191-212.
[16] H. M. Rietveld, *Phys Scripta* **2014**, *89*(9).
[17] A. Altomare, C. Cuocci, C. Giacovazzo, A. Moliterni, R. Rizzi, N. Corriero, A. Falcicchio, *J Appl Crystallogr* **2013**, *46*, 1231-1235.
[18] R. Rizzi, A. Altomare, *Crystals* **2020**, *10*(12).
[19] W. I. F. David, K. Shankland, *Acta Crystallogr A* **2008**, *64*, 52-64.
[20] R. Taniguchi, A. Inoue, M. Sayama, A. Uwamizu, K. Yamashita, K. Hirata, M. Yoshida, Y. Tanaka, H. E. Kato, Y. Nakada-Nakura, Y. Otani, T. Nishizawa, T. Doi, T. Ohwada, R. Ishitani, J. Aoki, O. Nureki, *Nature* **2017**, *548*(7667), 356-360.
[21] S. R. Pillai, M. Damaghi, Y. Marunaka, E. P. Spugnini, S. Fais, R. J. Gillies, *Cancer Metastasis Rev* **2019**, *38*(1-2), 205-222.
[22] R. J. Gillies, C. Pilot, Y. Marunaka, S. Fais, *Biochim Biophys Acta Rev Cancer* **2019**, *1871*(2), 273-280.
[23] E. P. Spugnini, S. Fais, *Expert Opin Ther Pat* **2020**, *30*(1), 15-25.
[24] D. Gnocchi, L. Del Coco, C. R. Girelli, F. Castellaneta, G. Cesari, C. Sabba, F. P. Fanizzi, A. Mazzocca, *Sci Rep* **2021**, *11*(1), 1259.
[25] A. Altomare, G. Campi, C. Cuocci, L. Eriksson, C. Giacovazzo, A. Moliterni, R. Rizzi, P. E. Werner, *J Appl Crystallogr* **2009**, *42*, 768-775.
[26] A. Altomare, C. Cuocci, C. Giacovazzo, G. S. Kamel, A. Moliterni, R. Rizzi, *Acta Crystallogr A* **2008**, *64*, 326-336.
[27] A. Altomare, C. Cuocci, C. Giacovazzo, A. Moliterni, R. Rizzi, *J Appl Crystallogr* **2012**, *45*, 789-797.
[28] A. Altomare, N. Corriero, C. Cuocci, A. Falcicchio, R. Rizzi, *Crystals* **2020**, *10*(1).
[29] J. L. Banks, H. S. Beard, Y. X. Cao, A. E. Cho, W. Damm, R. Farid, A. K. Felts, T. A. Halgren, D. T. Mainz, J. R. Maple, R. Murphy, D. M. Philipp, M. P. Repasky, L. Y. Zhang, B. J. Berne, R. A. Friesner, E. Gallicchio, R. M. Levy, *J Comput Chem* **2005**, *26*(16), 1752-1780.
[30] S. Genheden, U. Ryde, *Expert Opin Drug Dis* **2015**, *10*(5), 449-461.
[31] A. Carocci, M. Roselli, R. Budriesi, M. Micucci, J. F. Desaphy, C. Altamura, M. M. Cavalluzzi, M. Toma, G. I. Passeri, G. Milani, A. Lovece, A. Catalano, C. Bruno, A. De Palma, F. Corbo, C. Franchini, S. Habtemariam, G. Lentini, *Chemmedchem* **2021**, *16*(3), 578-588.
[32] T. A. Halgren, *J Comput Chem* **1996**, *17*(5-6), 520-552.
[33] A. D. Becke, *Phys Rev A* **1988**, *38*(6), 3098-3100.
[34] E. R. Davidson, D. Feller, *Chem Rev* **1986**, *86*(4), 681-696.
[35] A. W. Lange, J. M. Herbert, *J Chem Phys* **2010**, *133*(24).
[36] A. W. Lange, J. M. Herbert, *Chem Phys Lett* **2011**, *509*(1-3), 77-87.

Entry for the Table of Contents

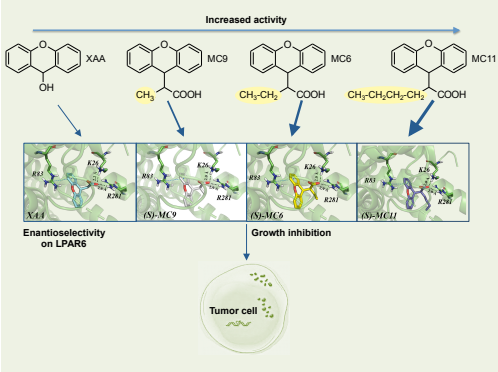

Xanthenylacetic acid (XAA) derivatives effectively inhibit hepatocellular carcinoma cell growth by targeting lysophosphatidic acid receptor 6 (LPAR6) in an enantioselective manner. Our results bring original insights on the characteristics of the LPAR6 binding site and on the chemico-physical properties of the novel LPAR6 antagonists. This will drive the design of more efficient LPAR6 antagonists expanding the therapeutic tools against HCC.